ADVANCED MATERIALS
www.advmat.de

Efficiency Roll-Off in Light-Emitting Electrochemical Cells

*Xiaoying Zhang, Joan Ràfols-Ribé, Jonas Mindemark, Shi Tang, Mattias Lindh, Eduardo Gracia-Espino, Christian Larsen, and Ludvig Edman**

Understanding "efficiency roll-off" (i.e., the drop in emission efficiency with increasing current) is critical if efficient and bright emissive technologies are to be rationally designed. Emerging light-emitting electrochemical cells (LECs) can be cost- and energy-efficiently fabricated by ambient-air printing by virtue of the in situ formation of a p-n junction doping structure. However, this in situ doping transformation renders a meaningful efficiency analysis challenging. Herein, a method for separation and quantification of major LEC loss factors, notably the outcoupling efficiency and exciton quenching, is presented. Specifically, the position of the emissive p-n junction in common singlet-exciton emitting LECs is measured to shift markedly with increasing current, and the influence of this shift on the outcoupling efficiency is quantified. It is further verified that the LEC-characteristic high electrochemical-doping concentration renders singlet-polaron quenching (SPQ) significant already at low drive current density, but also that SPQ increases super-linearly with increasing current, because of increasing polaron density in the p-n junction region. This results in that SPQ dominates singlet-singlet quenching for relevant current densities, and significantly contributes to the efficiency roll-off. This method for deciphering the LEC efficiency roll-off can contribute to a rational realization of all-printed LEC devices that are efficient at highluminance.

1. Introduction

Emerging electroluminescent technologies, in the form of the organic light-emitting diode (OLED) and the light-emitting electrochemical cell (LEC), are praised for their thin and flexible form factor,[1] the vibrant and tunable emission colors,[2] the non-glaring surface emission,[3] and the potential for energy- and cost-efficient fabrication.[4] A practical and sustainably relevant light-emission technology should preferably also deliver bright emission at high efficiency, but it is unfortunately common that the emission efficiency of OLED[5] and LEC[6] devices drops significantly with increasing drive current and luminance in a process generically termed "efficiency roll-off".

A functional route toward suppression of efficiency roll-off in OLEDs is through the employment of a carefully designed and exact multilayer device architecture, with the different layers, separately or in concert, providing for balanced injection of electrons and holes, facile electron and hole transport, unity electron and hole recombination into excitons, efficient conversion of excitons into photons, and efficient escape or "outcoupling" of the generated photons out of the device structure.[7] The excitons in organic semiconductors (OSCs) are termed singlets and triplets, and during electrical excitation they are formed in a singlet:triplet ratio of 1:3. Particular focus[5c] during OLED device design is on the attainment of balanced injection of electrons and holes, suppression of different types of exciton-exciton and exciton-polaron quenching (the electrons and holes in OSCs are termed polarons since they polarize their

X. Zhang, J. Ràfols-Ribé, S. Tang, E. Gracia-Espino, C. Larsen, L. Edman
The Organic Photonics and Electronics Group
Department of Physics
Umeå University
Umeå SE-90187, Sweden
E-mail: ludvig.edman@umu.se

J. Ràfols-Ribé, S. Tang, C. Larsen, L. Edman
LunaLEC AB
Umeå University
Umeå SE-90187, Sweden

J. Mindemark
Department of Chemistry – Ångström Laboratory
Uppsala University
Uppsala SE-751 21, Sweden

M. Lindh
Sustainable Resource Conversion unit, Biorefinery and Energy department, RISE Research Institutes of Sweden AB
Storgatan 65, Umeå SE-90330, Sweden

L. Edman
Wallenberg Initiative Materials Science for Sustainability
Department of Physics
Umeå University
Umeå SE-90187, Sweden

The ORCID identification number(s) for the author(s) of this article can be found under https://doi.org/10.1002/adma.202310156

DOI: 10.1002/adma.202310156

soft environment),[8] and on the generation of the photons at a position that enables efficient outcoupling. However, the unfortunate concomitant drawback is that the realization of such an exact multilayer architecture commonly requires fabrication by sequential thermal evaporation under high vacuum conditions, which is both expensive and wasteful with materials and energy.[9]

The LEC technology is formally distinguished from the OLED by the existence of mobile ions in the active material, where they are blended with the emissive OSC.[10] When a voltage is applied between the two electrodes that sandwich the active material, the mobile ions redistribute to enable the initial formation of electric double layers (EDLs) at the electrode interfaces and the subsequent electrochemical doping of the OSC. The electrochemical p-type (n-type) doping at the positive (negative) electrode constitutes injection of holes (electrons) and electrostatic compensatory motion of the mobile anions (cations) in the active material. The p-type and n-type doping regions grow until they make contact and form a p-n junction in the bulk of the active material. At this p-n junction, the injected electrons and holes recombine into excitons, which subsequently can decay under the emission of photons.[11]

The in situ formation of a p-n junction doping structure by electrochemical doping is attractive since it allows the utilization of air-stabile electrodes and a single-layer active material, which in turn has enabled energy- and cost-efficient printing and coating fabrication of complete LEC devices under ambient air.[12] However, the drawback with this in situ transformation is that it has rendered it difficult to pinpoint and quantify the different loss channels in LEC devices for a rational design of improved devices with suppressed efficiency roll-off. More specifically, although the formation of the EDLs and the p-n junction makes the electron and hole injection balanced and the electron and hole recombination to excitons perfect, respectively, in functional LECs, the difficulties in directly studying the dynamic p-n junction doping structure render it challenging to separate between, and quantify, the different losses due to various exciton quenching modes and poor outcoupling of the generated photons. Therefore, in order to enable an analysis of the efficiency roll-off in LECs it has been common to make the ad hoc assumption that the outcoupling efficiency of LECs is high (often 20%) and independent on the current density, which is a very questionable simplification in the light of recent results.[5c,6,13]

Here, we address this issue through the development of a methodology that first measures the evolution of the p-n junction doping structure with increasing current density, thereafter determines the corresponding changes in the optical outcoupling efficiency, and finally quantifies different exciton quenching losses as a function of the current density. We specifically investigate four archetypical singlet-exciton emitting LEC devices, distinguished by the ion-transporter and the active-material-thickness selection. We find that the general trend is that the emissive p-n junction shifts toward the anode with increasing current density, and that this shift is manifested in markedly deviating trends for the outcoupling efficiency between the different devices. With this understanding and information at hand, we can determine and separately quantify the losses due to singlet-polaron quenching (SPQ) and singlet-singlet quenching (SSQ) as a function of the current density. We specifically establish that SPQ dominates SSQ at all relevant current densities by more than two orders of magnitude, and that SPQ is increasing in a super-linear manner with the current density. The latter finding is rationalized by that the polaron concentration in the critical exciton-generating p-n junction region increases significantly with the current density. Importantly, this results in that an increasing fraction of the formed singlet excitons are impinging upon, and being quenched, by the polarons with increasing current density.

2. Results and Discussion

The emission efficiency of electroluminescent devices, such as OLEDs and LECs, is commonly quantified by the external quantum efficiency (EQE), which is the ratio between the number of photons exiting the device structure and the number of electrons entering the driving circuit.[6a,14] The EQE can be described by the following equation.

$$\mathrm{EQE} = \eta_{\mathrm{exc,form}} \times \left(1 - \eta_{\mathrm{exc,loss}}\right) \times \eta_{\mathrm{exc,rad}} \times \eta'_{\mathrm{out}} \quad (1)$$

The first $\eta_{\mathrm{exc,form}}$ factor is the exciton formation efficiency, that is, the ratio between the number of generated excitons in the active material and the number of electrons in the driving circuit; it specifically depends upon the electron and hole injection balance and on the efficiency with which electrons and holes recombine into excitons. The second $(1 - \eta_{\mathrm{exc,loss}})$ factor accounts for exciton losses due to bimolecular interactions in the form of the quenching of excitons by interactions with polarons or other excitons. The third $\eta_{\mathrm{exc,rad}}$ factor is the fraction of excitons that can emit light, which is 0.25 for a singlet emitter and 1 for a triplet emitter. The final η'_{out} factor represents the product of the photoluminescence quantum yield (PLQY) of the emitter and the outcoupling efficiency, with the latter being the quotient between the number of photons that exit the device structure and can be detected by an external observer and the number of photons generated in the active material.

As discussed in the introduction, the LEC-characteristic in situ formation of EDLs at the electrode interfaces and a p-n junction doping structure in the active-material bulk results in that the electron and hole injection are both efficient and balanced and that the recombination efficiency of electrons and holes into excitons is perfect. This in turn translates into that $\eta_{\mathrm{exc,form}}$ is equal to one (and independent of the drive current) for a functional LEC device.

The "excitonic loss factor" $\eta_{\mathrm{exc,loss}}$ accounts for losses due to, for example, exciton-polaron quenching and exciton-exciton quenching during the exciton lifetime. It has convincingly been demonstrated, by measurements and simulations, that exciton-polaron quenching is severe in single-OSC LEC devices, because of the characteristic high concentrations of polarons (formed by the in situ electrochemical doping) next to the p-n junction that results in their frequent encounters with the mobile excitons formed in the p-n junction region.[6f,15] It has further, more recently, been demonstrated that this issue can be alleviated through the employment of well-designed host-OSC:guest-OSC systems, which causes increased spatial separation of the exciton and polaron populations and the immobilization of the excitons on the guest OSC; but also that a correlated trade-off can be an increase in the

drive voltage.[6f,16] However, it is notable that it is currently unclear whether exciton-polaron quenching is a contributor to the efficiency roll-off, that is, whether the exciton-polaron quenching rate is increasing in a superlinear manner with increasing current density.

The third factor $\eta_{exc,rad}$ in Equation (1) is equal to 0.25 for the herein investigated LEC devices, which employ the singlet-emitting (fluorescent) conjugated polymer Super Yellow as the OSC emitter. The final η'_{out} factor is strongly dependent on the position of the emissive p-n junction in the interelectrode gap, since the radiative rate of the excitons, and thereby the PLQY, is affected by the Purcell effect,[17] and because the outcoupling of the generated photons in the active material is strongly influenced by optical microcavity effects,[18] self-absorption,[19] and on their proximity to doped regions and electrodes.

For our investigation of the efficiency roll-off in LECs, we have fabricated and investigated four different devices, which all feature a thin layer of active material sandwiched between a reflective Al cathode and a transparent indium-tin-oxide (ITO) anode. The active material is a blend of Super Yellow as the fluorescent OSC and the salt KCF_3SO_3 dissolved in a star-branched trimethylolpropane ethoxylate (TMPE) oligomeric ion transporter as the electrolyte. The devices were encapsulated with a transparent barrier in order to prohibit ambient-air-induced degradation,[20] and they were positioned on a heat sink during measurements to minimize obscuring effects from self-heating.[21] More details on the device fabrication and characterization can be found in the Experimental Section.

The four LEC devices are distinguished by two different end groups on the oligomeric TMPE-based ion transporter, being either a hydroxyl (TMPE-OH) or an octyl carbonate (TMPE-OC), and two different thicknesses of the active material.[22] The two LEC devices comprising TMPE-OH have an active-material thickness of 180 or 400 nm and are termed L1-thin and L1-thick, respectively, while the two LECs based on TMPE-OC feature an active-material thickness of 130 or 260 nm and are designated as L2-thin and L2-thick, respectively.

The motivation for the ion-transporter selection is that the change from TMPE-OC to TMPE-OH in a similar LEC device has been demonstrated to result in a marked shift of the steady-state position of the emissive p-n junction from close-to-the-anode to the center of the active material.[23] This cathodic shift was rationalized by that the polar hydroxyl end groups of TMPE-OH induce electron traps on nearby Super Yellow polymer segments, which selectively lowers the electron mobility of Super Yellow.[23] The motivation for changing the thickness of the active material is that it is anticipated to result in a correlated change in the distance between the emissive p-n junction and the reflective electrode surface. Both the shift of the ion transporter and the adjustment of the active-material thickness can accordingly result in that the emissive p-n junction changes between positions of constructive and destructive interference within the optical microcavity defined by the two electrodes, which in turn will result in that the outcoupling efficiency (η'_{out} in Equation (1)) will change significantly.[18d,24]

Figure 1a–f presents the initial evolution of the driving voltage V (a,d), the forward luminance L (b,e), and the EQE (c,f) with time for pristine L1-thin (a-c) and L1-thick (d-f) devices during driving with different constant current densities of 10, 25, 50 mA cm^{-2} (see inset in Figure 1a). The corresponding transients for L2-thin and L2-thick are depicted in Figure S1, Supporting Information. We mention that a much smaller solid collection angle for the photons of 0.007 sr (in the normal direction of the device plane) was used for the measurement of the forward luminance and the electroluminescence (EL) spectrum in comparison to the entire forward hemisphere (i.e., $\approx 2\pi$ sr) for the EQE.

The square markers in Figure 1a,d and Figure S1a,d, Supporting Information indicate the time at which the minimum voltage was measured. We assign this as the time of "steady state", that is, the time at which the net ionic motion is zero and the ionic drift and diffusion currents are of equal magnitude but of opposite direction.[25] The consistent observation for all investigated LECs is that the driving voltage decreases during the initial constant-current operation up to the time of steady state. This is in agreement with that the initial voltage-induced ion redistribution first resulted in the formation of injection-facilitating EDLs at the electrode interfaces and subsequently in transport-enhancing electrochemical doping of the Super Yellow OSC. Accordingly, all four devices fulfill the baseline requirements of functional LEC operation.

Figure 1b,c shows that both the forward luminance and the EQE of L1-thin increase with time during the initial operation. This temporal improvement is in line with that the electron/hole injection balance improves (to become perfect) during the EDL formation and that the electron-and-hole-recombination-to-exciton efficiency thereafter improves (to become perfect) during the p-n junction formation. However, we call attention to that a deviating temporal behavior for the luminance and EQE transients is observed for L1-thick (Figure 1e,f), L2-thin (Figure S1b,c, Supporting Information), and L2-thick (Figure S1e,f, Supporting Information).

Figure 1g–i summarizes the steady-state values for the minimum drive voltage, the forward luminance, and the EQE as a function of the current density for the four LEC devices. The minimum drive voltage does, as expected, increase with both increasing current density and increasing active-material thickness. The steady-state forward luminance (Figure 1h) also exhibits the expected increase with increasing drive current density, but the very weak dependence for L1-thick (solid blue squares) is notable. Figure 1i presents the decrease of the EQE with increasing current density, that is, the emission-efficiency roll-off. We find that the efficiency roll-off is most severe for L1-thick (solid blue squares) at 64%, but that it is much smaller, and essentially zero at the higher current densities, for L2-thick (solid orange circles).

Figure 1j presents the normalized steady-state forward EL spectra of L1-thick at three current densities, with the corresponding data for the other three LEC devices depicted in Figure S2, Supporting Information. The trend is that the shape of the EL spectrum changes with the current density, as exemplified by that the EL peak of L1-thick redshifts by 17 nm, and that the full width at half maximum (FWHM) of its emission envelope increases from 99 to 149 nm, when the current density is increased by a factor of five. Figure S3, Supporting Information shows that the luminous intensity is highly non-Lambertian, that is, strongly dependent on the viewing angle, in particular for the L1-thick and L2-thin devices.

In this context, we remember that both the luminance, EQE, and EL spectral properties can change drastically by shifting

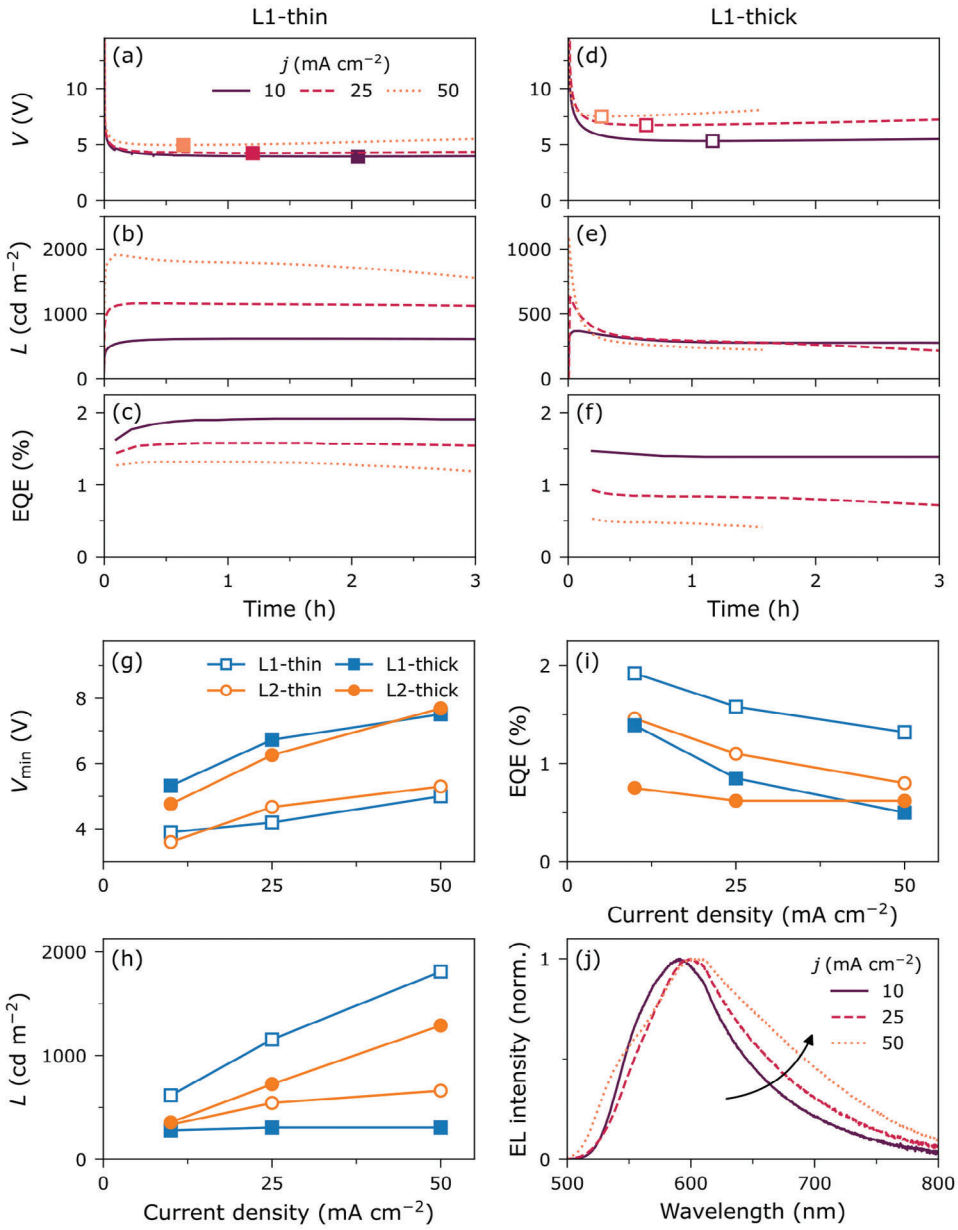

Figure 1. The temporal evolution of a,d) the voltage, b,e) the forward luminance, and c,f) the external quantum efficiency for representative pristine a–c) L1-thin and d–f) L1-thick devices, when driven by three different constant current densities, as identified in the inset of (a). The square markers in (a,d) indicate the time of minimum voltage, which is defined as the achievement of steady state. The steady-state values for g) the minimum voltage, h) the forward luminance, and i) the external quantum efficiency as a function of the current density for the four LEC devices, as identified in the inset of (g). j) The steady-state forward electroluminescence spectrum of L1-thick at three different current densities, as identified in the inset. The arrow indicates the spectral shift with increasing current density.

interference effects in thin-film devices, such as LECs and OLEDs. **Figure** 2a schematically visualizes this interference effect by presenting two light rays (solid red lines) that both originate from the same spot in the emissive p-n junction (the horizontal dotted black line), but which are distinguished by that one ray is directed so that it exits the device directly (through the transparent electrode and the transparent substrate) whereas the second ray is directed so that it is first reflected off the reflective electrode. If the optical path difference (including the phase shift during the reflection) between the two rays is equal to an integer (one-half or one-half plus an integer) of the emission wavelength, then the two rays will experience constructive (destructive) interference.

We have determined the position of the emissive p-n junction by a combined measurement and simulation of the EL spectrum and the EL intensity as a function of the viewing angle θ. The measurement was performed with a home-built spectrogoniometer setup (see Figure S4, Supporting Information), with the LEC device positioned on a temperature-controlled heat sink

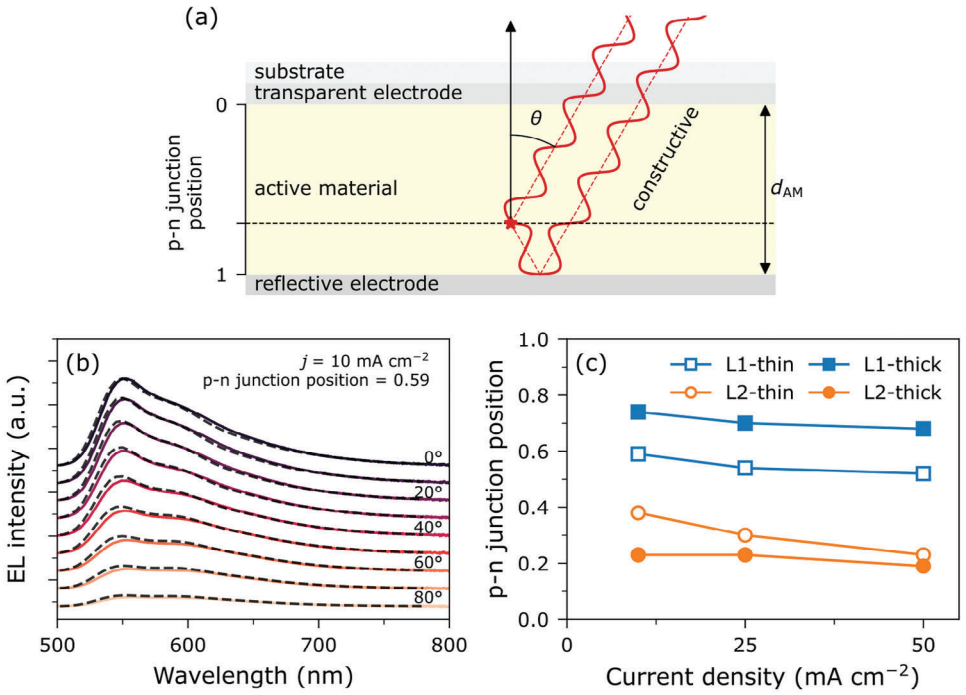

Figure 2. a) Schematic presentation of the optical interference between two light rays that originate from the same spot in the emissive p-n junction (horizontal dotted black line) in a thin-film LEC device, and which are solely distinguished by that one ray is directed directly out of the device through the transparent electrode and substrate, whereas the other ray is directed toward the reflective electrode and first after specular reflection exiting the device. Left part: the p-n junction position is defined to be 0 when located at the transparent electrode interface, and 1 when located at the reflective electrode interface. b) The measured (solid lines) and the best-fit simulated (dashed lines) EL spectra as a function of the viewing angle θ for L1-thin, as recorded at steady state with the device driven by a current density of 10 mA cm^{-2}. The derived best-fit value for the p-n junction position is 0.59. c) The steady-state position of the emissive p-n junction as a function of the current density for the four LEC devices, as identified in the inset.

to maintain a constant operational temperature of 298 K. The same viewing-angle dependent EL data was thereafter simulated, with the essential free parameter being the position of the emissive p-n junction. The left part of Figure 2a informs that a position value of 0 corresponds to a p-n junction at the transparent-electrode (ITO anode) interface, while a position of 1 represents a p-n junction at the reflective-electrode (Al cathode) interface. Thus, by identifying the set of simulated data that yields the best agreement with the measured data, it is possible to determine the position of the emissive p-n junction in the active material with high accuracy.[18d,23,24,26] The observed excellent agreement between the measured and the best-fit simulated data, as exemplified by a comparison of the solid lines with the dashed lines in Figure 2b, yields support for the validity of the procedure. More details on the measurement, simulation, and fitting procedures can be found in the Experimental Section.

Figure 2c presents a summary of the steady-state position of the emissive p-n junction as a function of the current density, with the different LECs identified in the upper inset. Interestingly, we find that the p-n junction position exhibits a significant dependency on the current density for all four LECs, with the general trend being that the p-n junction shifts toward the positive anode with increasing current density. It has previously been established that the steady-state position of the emissive p-n junction is determined by the electron/hole mobility ratio (while its initial position is determined by the cation/anion mobility ratio).[23,26] For instance, the steady-state p-n junction will be positioned in the center of the active material at equal electron and hole mobility, and shift toward the positive anode (negative cathode) if the electron (hole) mobility is higher. This yields that the emissive OSC Super Yellow in the herein investigated LECs exhibits a larger increase of the electron mobility than the hole mobility with increasing current density (and therefore electric field). We speculate that this asymmetry can be caused by that the electron traps are deeper than the hole traps.[27]

The observed positional shift of the emissive p-n junction with increasing current density (cf., Figure 2c) is important in the context of an emission-efficiency analysis since a change of the p-n junction doping structure can significantly affect η'_{out} and thereby EQE (see Equation (1)). We have therefore performed a systematic simulation of the effects of the changing p-n junction doping structure on η'_{out}, and **Figure 3**a presents one specific simulated doping structure (L1-thin at a drive current density of 25 mA cm^{-2}) as a visual guideline of the employed procedure.

The p-type and n-type doping regions were simulated with constant doping gradients, with the highest doping concentration at the electrode interfaces and zero concentration at the boundaries to the emissive p-n junction region. The total p-type and n-type doping concentrations were set equal because of charge conservation, which resulted in a larger gradient for the thinner doping region. The doping regions were discretized into ten layers with constant

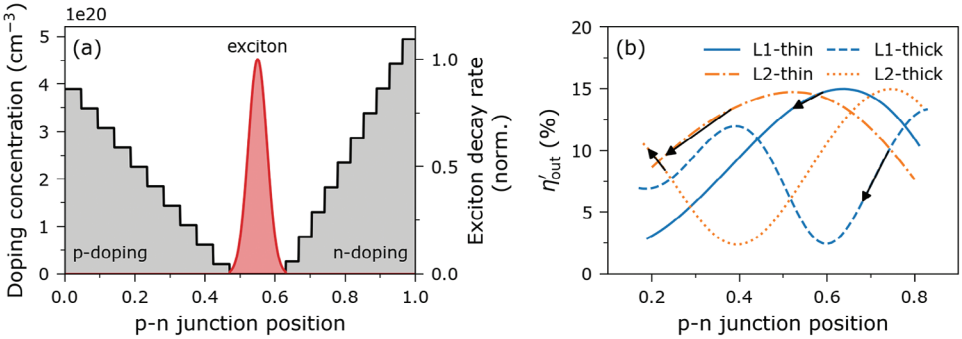

Figure 3. a) The simulated steady-state electrochemical p-type and n-type doping profiles and the exciton decay rate profile of L1-thin, with its p-n junction positioned at 0.55. b) The simulated outcoupling efficiency as a function of the position of the p-n junction for the four LEC devices. The thick black solid lines with arrows at the end indicate the observed shift of the steady-state p-n junction position (derived from Figure 2c) with increasing current density from 10 to 50 mA cm^{-2}.

doping concentration, and the associated wavelength- and doping-dependent complex refractive index of the emissive organic semiconductor Super Yellow was gleaned from ref. [28]. The electrons and holes recombine into excitons in the p-n junction, with a width of d_{pn} given by Equation (3) in the Experimental Section. The exciton decay rate as a function of position in the p-n junction region was modeled as a Gaussian, with a standard deviation of $d_{pn}/3$.[18d] This resulted in the formation of a minor (≈1%) fraction of excitons outside the transparent p-n junction region, which were removed from the simulation.[18d] The simulation of the four LECs at different drive current densities was adjusted as regards to the utilized active-material thickness and the observed center position of the emissive p-n junction (as gleaned from the data in Figure 2c). Figure 3a specifically displays the simulated doping structure for L1-thin with a steady-state p-n junction position of 0.55 (as resulting from it being driven by a current density of 25 mA cm^{-2}, see Figure 2c). Additional details on the simulation procedure can be found in the Experimental Section and in refs. [24,29].

Figure 3b presents the derived dependency of η'_{out} on the p-n junction position for the four different LECs, and the observed strongly undulating behavior is a direct manifestation of the interference (microcavity) effect depicted in Figure 2a. The thick black lines with an arrow at the end, positioned on top of the simulation traces, indicate the changes in η'_{out} that result from the observed shift of the position of the p-n junction, which in turn originated in the increase of the current density from 10 to 50 mA cm^{-2} (see Figure 2c). The importance of this shift is exemplified by that η'_{out} of L1-thick (dashed blue line) drops by a drastic 42% during the current-density increase, while L2-thick (dotted orange line) in contrast exhibits an increase in η'_{out} of 21% for the same change of the current density. Figure S5, Supporting Information presents a detailed 2D plot of the dependency of η'_{out}, as well as the substrate, self-absorption, waveguided, evanescent, and non-radiative modes, on both the active-material thickness and the p-n junction position.

Figure 4a,b summarizes the steady-state values for the measured EQE and the derived η'_{out}, respectively, as a function of the current density for the four LECs. With the aid of Equation (1), and by remembering that $\eta_{exc,form}$ is equal to 1 at steady state for an LEC device (with a fully formed p-n junction) and that $\eta_{exc,rad}$ is equal to 0.25 for the herein investigated singlet-emitting LECs, it is straightforward to derive the dependency of $\eta_{exc,loss}$ on the current density for the four LECs, as displayed by the symbol graphs in Figure 4c.

We first note that the four derived $\eta_{exc,loss}$ traces are notably more similar, from both a qualitative and a quantitative perspective, than the corresponding EQE and η'_{out} traces. More specifically, we find that $\eta_{exc,loss}$ increases monotonically with the current density for all four LECs, starting at 44–64% at the lowest current density of 10 mA cm^{-2} and reaching 61–76% at the highest current density of 50 mA cm^{-2}. We call particular attention to two important findings: i) $\eta_{exc,loss}$ is very high and thereby severely limits the EQE of the four LEC devices already at the relatively low current density of 10 mA cm^{-2}, and ii) $\eta_{exc,loss}$ exhibits a significant increase with increasing current density, which means that it is a major contributor to the efficiency roll-off in our LEC devices.

For a more detailed analysis, we remember that $\eta_{exc,loss}$ represents exciton losses due to bimolecular quenching interactions with polarons and other excitons during the exciton lifetime, and that it is only the singlet excitons that are emissive in the herein investigated LEC devices. In order to identify the main culprit of the quenching of the singlet excitons, we have performed a drift-diffusion simulation, with the two steady-state ion-concentration gradients being modeled as constants (cf., Figure 3a), the p-n junction being centered, and the other parameter values being gleaned from the scientific literature, as exemplified by the electron and hole mobility being 4×10^{-7} cm^2 V^{-1} s^{-1}, the singlet-polaron rate constant being 9×10^{-10} cm^3 s^{-1},[30] and the singlet-singlet rate constant being 2.8×10^{-8} cm^3 s^{-1}.[31] Additional information on the parameter selection and the simulation procedure can be found in Table S1, Supporting Information, and the Experimental Section.

Figure 4d presents the simulated steady-state concentration profiles for the hole-polarons (dotted lines to the left) and the electron-polarons (dashed lines to the right), as well as the singlet-exciton generation rate (solid lines), for the three current densities. As expected, we find that the exciton generation rate scales linearly with the current density and that the hole-polaron and electron-polaron concentration profiles are relatively independent of the current density (note the logarithmic y–axes). The latter is due to that the high polaron concentrations are effectuated by the electrostatic screening of the (invariant) ion

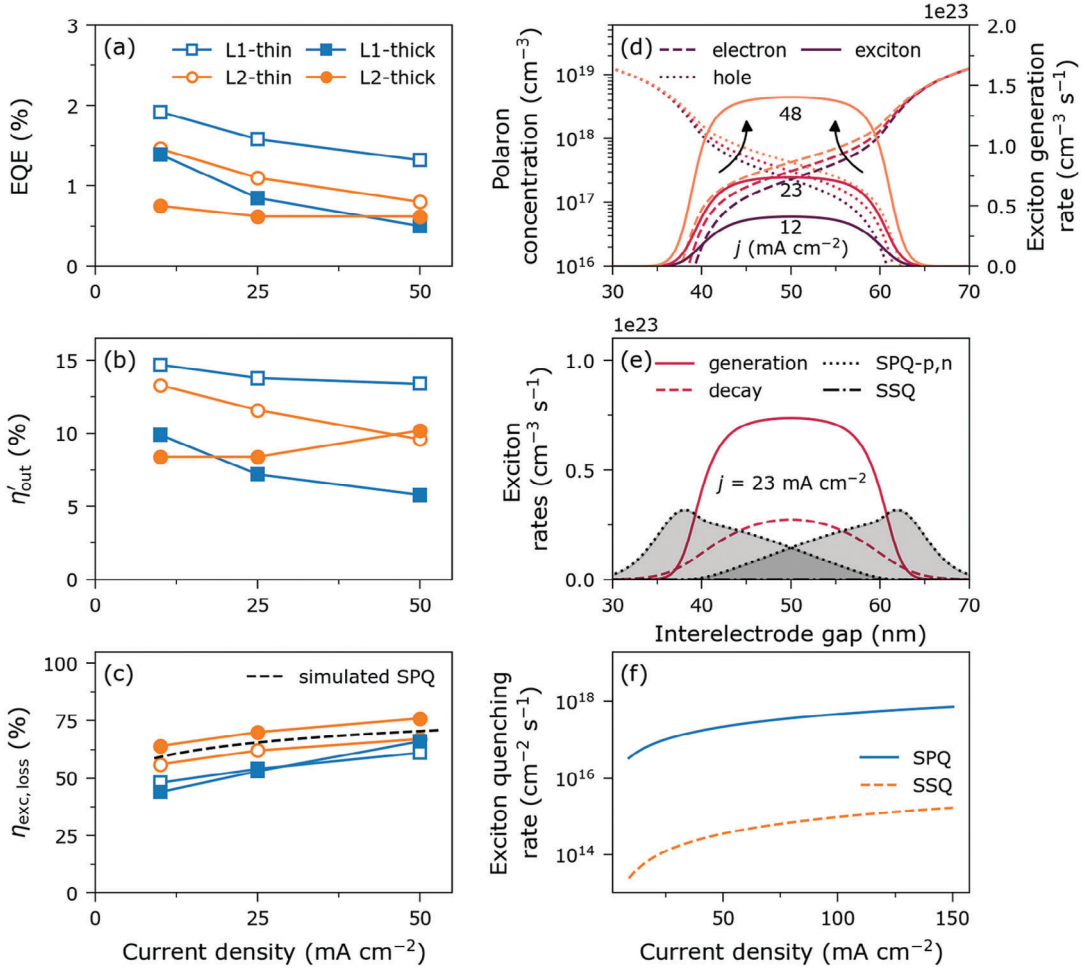

Figure 4. a) The measured external quantum efficiency, b) the outcoupling efficiency, and c) the derived (symbols) and the simulated (dashed line) excitonic loss factor as a function of the current density for the four LECs, as identified in the inset of (a). d) The simulated steady-state concentration profiles of the electron and hole polarons (left *y*–axis) and the exciton generation rate (right *y*–axis) at three different current densities, as specified next to the corresponding traces. e) The simulated exciton generation rate (solid red line), exciton decay rate (dashed red line), SPQ rate (dotted black line), and SSQ rate (dash-dotted black line) for a current density of 23 mA cm^{-2}. f) The simulated steady-state SPQ and SSQ rates as a function of the current density. The simulated LECs featured a centered p-n junction and an active-material thickness of 100 nm.

concentration profiles. We do however call attention to the marked increase of the (non-ion-compensated and thereby space-charge forming) electron and hole concentrations within the p-n junction region with increasing current density.

Figure 4e focuses on the singlet-exciton action in the p-n junction region, specifically the singlet-exciton generation rate (solid red line), the singlet-exciton decay rate (dashed red line), the SPQ rate (dotted black line), and the SSQ rate (dash-dotted black line) for a current density of 23 mA cm^{-2}. The fact that the generation rate does not exactly equal the combined decay and quenching rates is due to that the generated excitons diffuse to new locations during their lifetime. Figure 4f presents the simulated SPQ rate (solid blue line) and the SSQ rate (dashed orange line) on a log scale as a function of the current density; the corresponding data on a linear scale are displayed in Figure S6, Supporting Information.

Figure 4f reveals that SPQ dominates SSQ by two orders of magnitude for all device-relevant values for the current density. The notion that losses due to SSQ are insignificant is further supported by an estimate of the average distance between the emissive singlet excitons in the p-n junction region by:

$$d_{ss} \approx \left(\frac{e \times d_{pn}}{j \times \tau_s} \right)^{1/3} \quad (2)$$

where e is the elementary charge, d_{pn} is the effective width of the emissive p-n junction, j is the current density, and τ_s is the singlet-exciton lifetime. By implementing values of $d_{pn} = 20$ nm, $j = 50$ mA cm^{-2}, and $\tau_s = 2$ ns, we find that d_{ss} is ≈150 nm, which is much larger than the typical diffusion length of ≈10 nm for singlet excitons in organic semiconductors.[32] Thus, the short lifetime of the emissive singlets in Super Yellow prohibits the accumulation of SSQ-detrimental singlet-exciton densities at practical current densities.

SPQ is in contrast found to be a severe efficiency limiter. We present the spatially integrated SPQ losses as a function of the current density in the form of the dashed black line in Figure 4c. Interestingly, we find that the simulated SPQ loss trace replicates the four derived $\eta_{exc,loss}$ traces in Figure 4c with good accuracy. This implies that SPQ is the dominant exciton quenching mechanism in the four investigated singlet-emitting LECs.

The observation that remains to explain is why SPQ is becoming increasingly important with increasing current density, and a significant contributor to the efficiency roll-off (cf., Figure 4c). In other words, why is the SPQ rate increasing in a superlinear manner with the current density (cf., Figure S6, Supporting Information)? The mechanistic origin of SPQ is the excitation of a polaron to a higher energy state through the absorption (i.e., the loss) of a singlet exciton. The superlinear increase of SPQ with the current density thus yields that the polaron concentration at the exciton locations, that is, the p-n junction region, must increase with increasing current density. Interestingly, a detailed inspection of Figure 4d reveals that the simulated polaron concentration in the p-n junction region actually does increase (albeit from a modest value) with increasing current density. This qualitative argumentation is supported by that Figure 4e shows that the SPQ quenching is most prominent at the edges of the p-n junction region, at which the product of the polaron concentration and the exciton generation is at its highest values, and that the simulated SPQ trace in Figure 4f was best fitted with a $\propto j^{1.1}$ (and not a $\propto j$) equation (see Figure S6, Supporting Information).

We finally note that the two devices with the p-n junction positioned closest to the positive anode, that is, L2-thin and L2-thick (see Figure 2c), feature higher overall $\eta_{exc,loss}$ values in Figure 4c, and note that this is in agreement with that p-type doped Super Yellow has been measured to be a stronger singlet-exciton quencher than n-type doped Super Yellow.[19a,28,33] However, this mechanistic detail was, for clarity, not implemented in the simulated SPQ trace in Figure 4c (dashed line), which considered the SPQ rate constants for hole- and electron-polarons equal. Regardless, the major take-home message is that SPQ is both an overall limiting factor of the emission efficiency in singlet-emitting LECs and a significant contributor to the efficiency roll-off.

We conclude with a number of general comments and recommendations. First, it is a common practice to drive LEC devices with quickly pulsed current or voltage schemes in order to attain maximized EQE values.[6a,34] As these on-off schemes will prohibit the attainment of a steady-state doping profile, it is plausible that the polaron density in the exciton-generating p-n junction regime will be suppressed. This will, according to the herein-derived findings, result in a lowering of the SPQ and thereby explain the improved EQE and suppressed efficiency roll-off. However, the concomitant drawbacks are that the drive voltage is expected to increase when the polaron concentration decreases in the most resistive part of the device (viz., the p-n junction) and that a pulsed driving protocol can be challenging to practically implement in portable applications. Nevertheless, it is our ambition to return with a corresponding analysis of the efficiency roll-off in pulsed LECs using the herein-derived methodology.

Second, the efficiency roll-off is commonly quantified by the parameter J_0, which is the critical current density at which the EQE has dropped to half its peak value, EQE_{peak}.[35] This parameter is both practically relevant for applications and yields valuable input on the exciton quenching mechanism in OLED devices with stabile doping profiles. The latter analysis is however not recommended for LECs since their doping profile can feature a very strong dependency on the driving current or voltage. This is exemplified by that Figure 4a shows that the directly derived J_0 value for L2-thick is much higher (>50 mA cm^{-2}) than that of L1-thick (at ≈25 mA cm^{-2}), despite the exciton quenching mechanism being similar.

3. Conclusions

We introduce a generic methodology for the analysis of the different loss channels in effect in LEC devices during operation and exploit this new tool for the detailed analysis of the efficiency roll-off in common conjugated-polymer LECs. We specifically find that the position of the emissive p-n junction in these devices shifts markedly with increasing current density, and, through combined experimentation and modeling, show that these shifts are concomitant with largely deviating changes in the outcoupling efficiency. We further verify that the LEC-characteristic high electrochemical-doping concentration renders singlet-exciton-polaron quenching significant already at low drive current density. We finally find that this loss factor increases in a super-linear manner with increasing current density, and thereby is a major contributor to the efficiency roll-off, because of increasing polaron concentration in the emissive p-n junction region. We anticipate that this method development and elucidation of the primary LEC loss channels can help enable a rational lowering of the efficiency roll-off, and thereby pave the way for the design and development of LEC devices that deliver bright emission at high efficiency.

4. Experimental Section

Materials and Inks: The electroluminescent organic semiconductor was a phenyl-substituted poly (paraphenylene vinylene) conjugated copolymer termed "Super Yellow" (average repeat unit: 338 g mol^{-1}, M_n > 400 000 g mol^{-1}, M_w >1 300 000 g mol^{-1}, trade name: PDY-132, Merck, Darmstadt, GER), the salt was KCF_3SO_3 (purity > 98%, Sigma-Aldrich, USA), and the ion transporter was trimethylolpropane ethoxylate (TMPE), which was end-capped with either hydroxyls (TMPE-OH, M_n = 450 g mol^{-1}, Sigma-Aldrich, USA) or n-octyl carbonates (TMPE-OC, M_n = 918 g mol^{-1}). The synthesis of TMPE-OC is described in ref. [36]. The salt and the ion transporters were dried in a vacuum oven at 190 and 50 °C, respectively, for 12 h before the preparation of inks, while Super Yellow was used as received. The active-material constituents were separately dissolved in cyclohexanone (purity ≥99.5%, Sigma-Aldrich, USA) in the following concentrations: KCF_3SO_3 and TMPE-OH/TMPE-OC: 10 g l^{-1}; Super Yellow: 10–15 g l^{-1}; the higher Super Yellow concentration resulted in a thicker active-material film. These master solutions were stirred on a magnetic hot plate at 70° for ≥12 h before further processing. The active-material inks were prepared by blending the master inks in a mass ratio of Super Yellow:TMPE-OH:KCF_3SO_3 = 1:0.1:0.03 for L1-thin and L1-thick and Super Yellow:TMPE-OC:KCF_3SO_3 = 1:0.2:0.03 for L2-thin and L2-thick. The active-material inks were stirred on a hot plate at 70 °C for ≥ 6 h before further use.

Device Fabrication: The LEC devices were fabricated on transparent ITO-coated glass substrates (ITO thickness = 145 nm, R_s = 20 Ω $\square^{-1}$, glass thickness = 0.70 mm, substrate area = 30.0 × 30.0 mm^2, Thin Film Devices, USA). The ITO substrates were cleaned by sequential ultrasonic treatment in detergent (Extran MA 01, Merck, GER), deionized water, acetone, and isopropanol, followed by drying in an oven at 120 °C for ≥1 h. The

active-material ink was spin-coated (ramp-up time = 1 s, spinning time = 120 s) on the ITO, and thereafter dried at 70 °C for 1 h. The dry thickness of the active material (d_{AM}), as measured with a stylus profilometer (DektakXT, Bruker), was controlled by the spin speed and the Super Yellow concentration as follows: L1-thin = 10 g L^{-1} and 2300 rpm; L1-thick = 15 g L^{-1} and 2000 rpm; L2-thin = 10 g L^{-1} and 3000 rpm; L2-thick = 15 g L^{-1} and 2700 rpm. The reflective Al top electrode (thickness = 100 nm) was deposited by thermal evaporation under vacuum ($p < 8 \times 10^{-6}$ mbar) through a shadow mask. The overlap of the transparent ITO anode and the reflective Al cathode defined four independent 2.0 × 2.0 mm^2 LEC devices on each substrate. The LECs were finally protected from the ambient air by attaching a thin glass lid on top of the Al cathodes, using either a UV-curable epoxy (E132, Ossila) that was cured for 15 min (UV-Exposure Box 1, Gie-Tec GmbH) (L1-thin, L1-thick, L2,-thick),[20b] or a 12-micrometer-thick PSA film (L2-thin). The ink preparation and device fabrication were performed in N_2-filled gloveboxes ($[O_2] < 1$ ppm, $[H_2O] < 1$ ppm).

Device Characterization: The LEC devices were positioned on a temperature-controlled heat sink, comprising an Al-plate/thermal-paste/soft-thermal-pad three-layer structure on top of a Peltier element, which established a device temperature of 298 K also at the highest driving current density.[37] The LEC devices were driven by a constant current density, with the compliance voltage set to 21 V, and with ITO biased as the positive anode. A source-measure unit (Keithley 2400) supplied the current and recorded the corresponding voltage. 33 independent devices were measured in total, and the presented data were for the representative devices within this set.

The angle-resolved electroluminescence (EL) intensity and spectrum of the LEC devices were measured with a custom-built, automated spectrogoniometer setup, as schematically depicted in Figure S4, Supporting Information. The device under study was placed in a connection jig, which aligned the emission area of the device with the rotation axis of a stepper motor. This rotation defined the viewing angle of the device, with 0° corresponding to the forward emission. The viewing angle was controlled by a Python-based virtual instrument and varied between −80° and 80° in steps of 5° or 10°. A fraction of the device emission was collected by a collimating lens (∅ = 7.2 mm, F230 SMA-A, Thorlabs, Germany) positioned 75 mm away from the device, resulting in a small and constant solid collection angle of 0.007 sr. An optical fiber delivered the collected light to a CCD-array spectrometer (Flame-S, Ocean Optics, US). More details on the measurement setup and procedure can be found in ref. [18d].

Modeling: The modeling was executed with a commercial software (Setfos, versions 5.1/5.3 Fluxim AG, CH). The simulated LEC device structure comprised, from top to bottom, the glass substrate (thickness d = 0.70 mm), the ITO anode (d = 145 nm), the active material (thickness dependent on experiment), and the Al cathode (d = 100 nm). The excitons were modeled as emissive electrical dipoles. The simulation of the EL spectra and the EL intensity, for the determination of the emissive p-n junction position, was executed with the exciton distribution being a delta function, positioned in a transparent and non-doped active material using the wavelength-dependent refractive index of pristine Super Yellow.[28] It has been demonstrated that the accurate determination of the p-n junction position is effectively invariant to these simplifications in refs. [23,29].

For the simulation of the outcoupling efficiency and optical losses, the active material was divided into three sublayers: a p-type doped region and a n-type doped region that sandwiched an emissive and transparent p-n junction region. The doped regions were modeled with constant doping gradients, and the total number of dopants in the p-type and n-type regions was set equal because of charge conservation. The doping regions were discretized into ten layers with constant doping concentration, and the associated wavelength- and doping-dependent complex refractive index of the emissive organic semiconductor Super Yellow was gleaned from refs. [24,28,29]. The p-n junction width (d_{pn}) was determined by:

$$d_{pn} = K(c_1 + c_2 d_{AM})^{2/3} \quad (3)$$

where the derived values of the constants are K = 17.4 nm $V^{-2/3}$, c_1 = 0.12 V and c_2 = 0.011 V nm^{-1}.[24] The electrons and holes recombine into excitons in the p-n junction, and the exciton formation distribution in the p-n junction region was modeled as a Gaussian with a width determined by its standard deviation of $d_{pn}/3$. This resulted in the generation of a minor (≈1%) fraction of the excitons outside the transparent p-n junction region, and these were removed from the simulation.[18d] The modeling of the four LECs at different drive current densities was adjusted as regards to the derived center position of the emissive p-n junction, as gleaned from the data in Figure 2c.

The drift-diffusion simulations, for the determination of the steady-state spatial profiles for the hole-polarons, the electron-polarons, the exciton generation rate, the exciton decay rate, the SPQ rate, and the SSQ rate as a function of the current density, were performed with an active-material thickness of 100 nm and a centered p-n junction. The p-n junction width was determined with Equation (3). The steady-state ion profiles were implemented in the form of immobile donor/acceptor distributions, with constant and symmetric gradients. All excitons were formed and remained in the singlet state, which excludes polaron and exciton interactions with the (dark) triplet state. The SPQ and SSQ rates were integrated over the width of the p-n junction and were accordingly presented with the unit of per square centimeter and second. The ohmic injection of electrons and holes that result from the EDL formation at the two electrode interfaces in LEC devices was mimicked by using small and symmetric injection barriers of 0.1 eV. The detailed parameter selection is listed in Table S1, Supporting Information and is similar to those reported in refs. [23,26].

Statistical Analysis: In total, 33 different LEC devices were prepared and measured. The observed variation of the optoelectronic and spectral behavior of the four different device categories (L1-thin, L1-thick, L2-thin, and L2-thick) was very minor. The displayed and discussed optoelectronic and spectral data were for the typical device of each category. The electroluminescence spectra in Figure 1f and the exciton generation rate in Figure 3a have been normalized.

Supporting Information

Supporting Information is available from the Wiley Online Library or from the author.

Acknowledgements

The authors wish to acknowledge generous financial support from the Swedish Research Council (2019-02345 and 2021-04778), the Swedish Energy Agency (50779-1 and P2021-00032), "Bertil och Britt Svenssons stiftelse för belysningsteknik," Kempe Foundations, the Knut and Alice Wallenberg Foundation for a Proof of concept grant (KAW 2022.0381), the Wallenberg Initiative Materials Science for Sustainability (WISE) funded by the Knut and Alice Wallenberg Foundation (WISE-AP01-D02), and the European Research Council for an ERC Advanced Grant (project 101096650).

Conflict of Interest

The authors declare no conflict of interest.

Data Availability Statement

The data that support the findings of this study are available from the corresponding author upon reasonable request.

Keywords

efficiency roll-off, light-emitting electrochemical cell, p-n junction position, singlet-polaron quenching, singlet-singlet quenching

Received: September 30, 2023
Revised: December 28, 2023
Published online: January 17, 2024

[1] a) K. Schlingman, Y. Chen, R. S. Carmichael, T. B. Carmichael, *Adv. Mater.* **2021**, *33*, 2006863; b) S. R. Forrest, *Nature* **2004**, *428*, 911.
[2] a) Z. Shen, P. E. Burrows, V. Bulovic, S. R. Forrest, M. E. Thompson, *Science* **1997**, *276*, 2009; b) H.-C. Su, Y.-R. Chen, K.-T. Wong, *Adv. Funct. Mater.* **2020**, *30*, 1906898.
[3] a) C. Garditz, R. Patzold, D. Buchhauser, J. Wecker, A. Winnacker, presented at Conf. on Organic Optoelectronics and Photonics II, Strasbourg, April **2006**. b) J. W. Park, D. C. Shin, S. H. Park, *Semicond. Sci. Technol.* **2011**, *26*, 034002.
[4] a) A. Sandström, L. Edman, *Energy Technol.* **2015**, *3*, 329; b) Y. Zhou, C. Fuentes-Hernandez, J. Shim, J. Meyer, A. J. Giordano, H. Li, P. Winget, T. Papadopoulos, H. Cheun, J. Kim, M. Fenoll, A. Dindar, W. Haske, E. Najafabadi, T. M. Khan, H. Sojoudi, S. Barlow, S. Graham, J.-L. Brédas, S. R. Marder, A. Kahn, B. Kippelen, *Science* **2012**, *336*, 327.
[5] a) Y. Wang, Y. Zhu, G. Xie, H. Zhan, C. Yang, Y. Cheng, *J. Mater. Chem. C* **2017**, *5*, 10715; b) N. C. Giebink, B. W. D'Andrade, M. S. Weaver, P. B. Mackenzie, J. J. Brown, M. E. Thompson, S. R. Forrest, *J. Appl. Phys.* **2008**, *103*, 044509; c) C. Murawski, K. Leo, M. C. Gather, *Adv. Mater.* **2013**, *25*, 6801; d) M. A. Baldo, D. F. O'brien, Y. You, A. Shoustikov, S. Sibley, M. E. Thompson, S. R. Forrest, *Nature* **1998**, *395*, 151.
[6] a) D. Tordera, J. Frey, D. Vonlanthen, E. Constable, A. Pertegás, E. Ortí, H. J. Bolink, E. Baranoff, M. K. Nazeeruddin, *Adv. Energy Mater.* **2013**, *3*, 1338; b) S. Jenatsch, L. Wang, N. Leclaire, E. Hack, R. Steim, S. B. Anantharaman, J. Heier, B. Ruhstaller, L. Penninck, F. Nüesch, R. Hany, *Org. Electron.* **2017**, *48*, 77; c) S. Tang, P. Lundberg, Y. Tsuchiya, J. Ràfols-Ribé, Y. Liu, J. Wang, C. Adachi, L. Edman, *Adv. Funct. Mater.* **2022**, *32*, 2205967; d) P. Lundberg, Y. Tsuchiya, E. M. Lindh, S. Tang, C. Adachi, L. Edman, *Nat. Commun.* **2019**, *10*, 5307; e) P. Lundberg, E. M. Lindh, S. Tang, L. Edman, *ACS Appl. Mater. Interfaces* **2017**, *9*, 28810; f) S. Tang, A. Sandström, P. Lundberg, T. Lanz, C. Larsen, S. Van Reenen, M. Kemerink, L. Edman, *Nat. Commun.* **2017**, *8*, 1190.
[7] a) S.-J. Su, E. Gonmori, H. Sasabe, J. Kido, *Adv. Mater.* **2008**, *20*, 4189; b) S. Reineke, K. Walzer, K. Leo, *Phys. Rev. B* **2007**, *75*, 125328.
[8] C. Franchini, M. Reticcioli, M. Setvin, U. Diebold, *Nat. Rev. Mater.* **2021**, *6*, 560.
[9] a) H. Gorter, M. J. J. Coenen, M. W. L. Slaats, M. Ren, W. Lu, C. J. Kuijpers, W. A. Groen, *Thin Solid Films* **2013**, *532*, 11; b) J. Zimmermann, S. Schlisske, M. Held, J.-N. Tisserant, L. Porcarelli, A. Sanchez-Sanchez, D. Mecerreyes, G. Hernandez-Sosa, *Adv. Mater. Technol.* **2019**, *4*, 1800641.
[10] Q. Pei, G. Yu, C. Zhang, Y. Yang, A. J. Heeger, *Science* **1995**, *269*, 1086.
[11] a) Q. Pei, Y. Yang, G. Yu, C. Zhang, A. J. Heeger, *J. Am. Chem. Soc.* **1996**, *118*, 3922; b) P. Matyba, K. Maturova, M. Kemerink, N. D. Robinson, L. Edman, *Nat. Mater.* **2009**, *8*, 672.
[12] a) A. Sandström, H. F. Dam, F. C. Krebs, L. Edman, *Nat. Commun.* **2012**, *3*, 1002; b) A. Asadpoordarvish, A. Sandström, C. Larsen, R. Bollström, M. Toivakka, R. Österbacka, L. Edman, *Adv. Funct. Mater.* **2015**, *25*, 3238; c) J. Liang, L. Li, X. Niu, Z. Yu, Q. Pei, *J. Phys. Chem. C* **2013**, *117*, 16632; d) J. Zimmermann, L. Porcarelli, T. Rödlmeier, A. Sanchez-Sanchez, D. Mecerreyes, G. Hernandez-Sosa, *Adv. Funct. Mater.* **2018**, *28*, 1705795.
[13] a) K. Yasuji, T. Sakanoue, F. Yonekawa, K. Kanemoto, *Nat. Commun.* **2023**, *14*, 992; b) M. Lenes, G. Garcia-Belmonte, D. Tordera, A. Pertegás, J. Bisquert, H. J. Bolink, *Adv. Funct. Mater.* **2011**, *21*, 1581; c) Y.-C. Chiu, R.-H. Yi, T.-Y. Ou, D. Luo, J.-Y. Lien, Z.-P. Yang, C.-W. Lu, H.-C. Su, *Org. Electron.* **2021**, *88*, 106016; d) H. Iwakiri, H. Watanabe, Y. Noguchi, *ACS Appl. Electron. Mater.* **2021**, *3*, 2355.
[14] a) S. R. Forrest, D. D. C. Bradley, M. E. Thompson, *Adv. Mater.* **2003**, *15*, 1043; b) C. Coburn, J. Lee, S. R. Forrest, *Adv. Opt. Mater.* **2016**, *4*, 889; c) R. Yu, Y. Song, K. Zhang, X. Pang, M. Tian, L. He, *Adv. Funct. Mater.* **2022**, *32*, 2110623.
[15] S. Van Reenen, R. A. J. Janssen, M. Kemerink, *Adv. Funct. Mater.* **2015**, *25*, 3066.
[16] S. Tang, C. Larsen, J. Ràfols-Ribé, J. Wang, L. Edman, *Adv. Opt. Mater.* **2021**, *9*, 2002105.
[17] a) M. Furno, R. Meerheim, S. Hofmann, B. Lussem, K. Leo, *Phys. Rev. B* **2012**, *805*, 115205; b) C. X. Zang, S. H. Liu, M. X. Xu, R. F. Wang, C. Cao, Z. L. Zhu, J. M. Zhang, H. Wang, L. T. Zhang, W. F. Xie, C. S. Lee, *Light: Sci. Appl.* **2021**, *10*, 116.
[18] a) M. Diethelm, Q. Grossmann, A. Schiller, E. Knapp, S. Jenatsch, M. Kawecki, F. Nüesch, R. Hany, *Adv. Opt. Mater.* **2019**, *7*, 1801278; b) E. Fresta, R. D. Costa, *J. Mater. Chem. C* **2017**, *5*, 5643; c) M. C. Gather, S. Reineke, *J. Photonics Energy* **2015**, *5*, 057607; d) E. M. Lindh, P. Lundberg, T. Lanz, J. Mindemark, L. Edman, *Sci. Rep.* **2018**, *8*, 6970; e) H.-C. Su, *ChemPlusChem* **2018**, *83*, 197; f) T.-W. Wang, H.-C. Su, *Org. Electron.* **2013**, *14*, 2269.
[19] a) N. Kaihovirta, A. Asadpoordarvish, A. Sandström, L. Edman, *ACS Photonics* **2014**, *1*, 182; b) F. P. Wenzl, P. Pachler, E. J. W. List, D. Somitsch, P. Knoll, S. Patil, R. Guentner, U. Scherf, G. Leising, *Phys. E* **2002**, *13*, 1251.
[20] a) A. Asadpoordarvish, A. Sandström, L. Edman, *Adv. Eng. Mater.* **2016**, *18*, 105; b) A. Asadpoordarvish, A. Sandström, S. Tang, J. Granström, L. Edman, *Appl. Phys. Lett.* **2012**, *100*, 193508.
[21] a) J. Ràfols-Ribé, E. Gracia-Espino, S. Jenatsch, P. Lundberg, A. Sandström, S. Tang, C. Larsen, L. Edman, *Adv. Opt. Mater.* **2021**, *9*, 2001405; b) E. Fresta, J. Dosso, J. Cabanillas-Gonzalez, D. Bonifazi, R. D. Costa, *ACS Appl. Mater. Interfaces* **2020**, *12*, 28426.
[22] J. Mindemark, L. Edman, *J. Mater. Chem. C* **2016**, *4*, 420.
[23] J. Ràfols-Ribé, X. Zhang, C. Larsen, P. Lundberg, E. M. Lindh, C. T. Mai, J. Mindemark, E. Gracia-Espino, L. Edman, *Adv. Mater.* **2022**, *34*, 2107849.
[24] E. M. Lindh, P. Lundberg, T. Lanz, L. Edman, *Sci. Rep.* **2019**, *9*, 10433.
[25] S. Van Reenen, P. Matyba, A. Dzwilewski, R. A. J. Janssen, L. Edman, M. Kemerink, *J. Am. Chem. Soc.* **2010**, *132*, 13776.
[26] M. Diethelm, A. Schiller, M. Kawecki, A. Devižis, B. Blülle, S. Jenatsch, E. Knapp, Q. Grossmann, B. Ruhstaller, F. Nüesch, R. Hany, *Adv. Funct. Mater.* **2019**, *30*, 1906803.
[27] a) C. A. Amorim, M. R. Cavallari, G. Santos, F. J. Fonseca, A. M. Andrade, S. Mergulhão, *J. Non-Cryst. Solids* **2012**, *358*, 484; b) S. Gambino, A. K. Bansal, I. D. W. Samuel, *Org. Electron.* **2010**, *11*, 467.
[28] T. Lanz, E. M. Lindh, L. Edman, *J. Mater. Chem. C* **2017**, *5*, 4706.
[29] J. Ràfols-Ribé, C. Hänisch, C. Larsen, S. Reineke, L. Edman, *Adv. Mater. Technol.* **2023**, *8*, 2202120.
[30] E. J. W. List, C.-H. Kim, A. K. Naik, U. Scherf, G. Leising, W. Graupner, J. Shinar, *Phys. Rev. B* **2001**, *64*, 155204.
[31] P. E. Shaw, A. J. Lewis, A. Ruseckas, I. D. W. Samuel, in *Organic Photovoltaics VII*, (Eds.: Z. H. Kafafi, P. A. Lane), SPIE, Bellingham, WA **2006**, Vol. *6334*, p. 63340G.
[32] P. E. Shaw, A. Ruseckas, I. D. W. Samuel, *Adv. Mater.* **2008**, *20*, 3516.
[33] S. Van Reenen, M. V. Vitorino, S. C. J. Meskers, R. A. J. Janssen, M. Kemerink, *Phys. Rev. B* **2014**, *89*, 205206.
[34] a) M.-L. Wu, G.-Y. Chen, T.-A. Shih, C.-W. Lu, H.-C. Su, *Phys. Chem. Chem. Phys.* **2018**, *20*, 18226; b) N. M. Shavaleev, R. Scopelliti, M. Grätzel, M. K. Nazeeruddin, A. Pertegás, C. Roldán-Carmona, D. Tordera, H. J. Bolink, *J. Mater. Chem. C* **2013**, *1*, 2241; c) G. E. Schneider, A. Pertegás, E. C. Constable, C. E. Housecroft, N. Hostettler, C. D. Morris, J. A. Zampese, H. J. Bolink, J. M. Junquera-Hernández, E. Ortí, M. Sessolo, *J. Mater. Chem. C* **2014**, *2*, 7047; d) T. Sakanoue, J. Li, H. Tanaka, R. Ito, S. Ono, S.-I. Kuroda, T. Takenobu, *Adv. Mater.* **2017**, *29*, 1606392.
[35] M. A. Baldo, C. Adachi, S. R. Forrest, *Phys. Rev. B* **2000**, *62*, 10967.
[36] J. Mindemark, S. Tang, J. Wang, N. Kaihovirta, D. Brandell, L. Edman, *Chem. Mater.* **2016**, *28*, 2618.
[37] J. Ràfols-Ribé, N. D. Robinson, C. Larsen, S. Tang, M. Top, A. Sandström, L. Edman, *Adv. Funct. Mater.* **2020**, *30*, 1908649.